

The effect of laser entrance hole foil thickness on MagLIF-relevant laser preheat

Cite as: Phys. Plasmas **27**, 113301 (2020); <https://doi.org/10.1063/5.0021034>

Submitted: 07 July 2020 . Accepted: 15 October 2020 . Published Online: 05 November 2020

 A. J. Harvey-Thompson,  M. R. Weis,  D. E. Ruiz,  M. S. Wei, A. B. Sefkow, T. Nagayama,  E. M. Campbell, J. A. Fooks,  M. E. Glinsky, and  K. J. Peterson

COLLECTIONS

 This paper was selected as an Editor's Pick



View Online



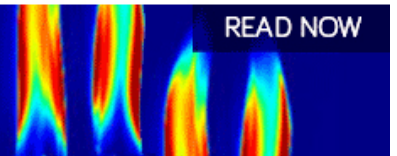
Export Citation



CrossMark

AIP Advances
Fluids and Plasmas Collection

READ NOW



The effect of laser entrance hole foil thickness on MagLIF-relevant laser preheat

Cite as: Phys. Plasmas **27**, 113301 (2020); doi: [10.1063/5.0021034](https://doi.org/10.1063/5.0021034)

Submitted: 7 July 2020 · Accepted: 15 October 2020 ·

Published Online: 5 November 2020



View Online



Export Citation



CrossMark

A. J. Harvey-Thompson,^{1,a)}  M. R. Weis,¹  D. E. Ruiz,¹  M. S. Wei,²  A. B. Sefkow,² T. Nagayama,¹
E. M. Campbell,²  J. A. Fooks,³ M. E. Glinsky,¹  and K. J. Peterson¹ 

AFFILIATIONS

¹Sandia National Laboratories, P.O. Box 5800, Albuquerque, New Mexico 87185, USA

²Laboratory for Laser Energetics, University of Rochester, Rochester, New York 14623-1299, USA

³General Atomics, P.O. Box 85608, San Diego, California 92186, USA

^{a)} Author to whom correspondence should be addressed: ajharve@sandia.gov

ABSTRACT

The magnetized liner inertial fusion (MagLIF) scheme relies on coupling laser energy into an underdense fuel raising the fuel adiabat at the start of the implosion. To deposit energy into the fuel, the laser must first penetrate a laser entrance hole (LEH) foil which can be a significant energy sink and introduce mix. In this paper, we report on experiments investigating laser energy coupling into MagLIF-relevant gas cell targets with LEH foil thicknesses varying from 0.5 μm to 3 μm . Two-dimensional (2D) axisymmetric simulations match the experimental results well for 0.5 μm and 1 μm thick LEH foils but exhibit whole-beam self-focusing and excessive penetration of the laser into the gas for 2 μm and 3 μm thick LEH foils. Better agreement for the 2 μm -thick foil is found when using a different thermal conductivity model in 2D simulations, while only 3D Cartesian simulations come close to matching the 3 μm -thick foil experiments. The study suggests that simulations may over-predict the tendency for the laser to self-focus during MagLIF preheat when thicker LEH foils are used. This effect is pronounced with 2D simulations where the azimuthally symmetric density channel effectively self-focuses the rays that are forced to traverse the center of the plasma. The extra degree of freedom in 3D simulations significantly reduces this effect. The experiments and simulations also suggest that, in this study, the amount of energy coupled into the gas is highly correlated with the laser propagation length regardless of the LEH foil thickness.

Published under license by AIP Publishing. <https://doi.org/10.1063/5.0021034>

I. INTRODUCTION

Magnetized Liner Inertial Fusion (MagLIF)¹ is a magnetized inertial confinement fusion (ICF) scheme that has produced fusion-relevant conditions² by imploding a cylindrical liner containing fuel typically using a pulsed power driver. MagLIF overcomes the challenges associated with the cylindrical geometry most natural to pulsed power and relatively long implosion times (~ 100 ns) by employing fuel pre-magnetization and fuel preheat. Pre-magnetizing the fuel reduces radial thermal conduction, limiting energy losses during the long implosion, and the compression of the magnetic field results in field strengths at stagnation that are sufficient to trap alpha particles along the cylindrical axis. The fuel is preheated at the start of the implosion to raise the adiabat of the fuel allowing the implosion to do more PdV work, overcoming the relatively inefficient compression of cylindrical (compared to spherical) implosions. Fuel preheat requires that kilojoules of energy be deposited into the fuel within the target volume without introducing contaminants that could contribute to

unacceptable radiative losses during the relatively long implosion.³ At Sandia National Laboratories, this is achieved by using a long-pulse (2–6 ns) 527 nm laser of moderate intensity (order of 10^{14} W cm⁻²) to deposit energy via inverse bremsstrahlung absorption into the underdense ($n_e/n_{\text{crit}} \leq 0.1$) gaseous fusion fuel. While this process is generally well understood,⁴ it is complicated by the need for the laser to first penetrate through a laser entrance hole (LEH) polyimide foil window that is used to contain the gas and by laser plasma instabilities (LPI's).

The LEH foil plays a significant role in MagLIF preheat by absorbing a substantial amount of laser energy⁵ and by being a source of material mix in MagLIF experiments.⁶ The LEH region is challenging to model during preheat because it begins initially well above supercritical density before undergoing rapid heating and expansion at the start of the laser pulse. The dynamics of this process can affect the amount of laser energy deposited in the foil material and the density profiles encountered by the incoming beam.

In spite of its importance, the laser–LEH interaction has not been sufficiently studied under conditions relevant to MagLIF. Other experiments that utilize gas-filled targets with LEH foils, such as hohlraums used in laser indirect drive inertial confinement fusion at the National Ignition Facility (NIF),^{7–9} have successfully simulated laser propagation⁹ in those targets. However, these experiments typically use a thinner material ($< 1 \mu\text{m}$ thick vs $1.5\text{--}3.5 \mu\text{m}$ thick current MagLIF experiments),^{5,10,11} higher laser energies (10's of kJ vs < 4 kJ for MagLIF), higher laser intensities ($> 1 \times 10^{14} \text{ W/cm}^2$), multiple beams, and shorter wavelength lasers ($\lambda = 351 \text{ nm}$ for NIF vs $\lambda = 527 \text{ nm}$ for MagLIF). Therefore, more data are needed closer to current MagLIF experimental parameters.

A previous study on the 3ω ($\lambda = 351 \text{ nm}$) OMEGA-EP laser used Ar-gas-filled MagLIF-like targets to investigate energy deposition into underdense gasses.¹² The observed time-gated x-ray self-emission profiles in the experiments were successfully reproduced with the radiation-hydrodynamic (RHD) code HYDRA,¹³ in particular the axial extent of the emission, which gave confidence that the code was able to reproduce the coupling of laser energy into the underdense gas. In those experiments, a relatively thin ($1 \mu\text{m}$ thick) LEH foil was used which, in simulations, only absorbed a small fraction of the incident laser energy ($< 8\%$). Because of this, the study did not provide a stringent test of how accurately the simulation model couples energy into thicker LEH foils (between 1.5 and $3.5 \mu\text{m}$) to contain the high pressure gas at the desired density (up to 120 psi, 1.4 mg/cm^3) that are used in typical MagLIF experiments.¹¹

The work presented in this paper aims to study the impact of LEH foil thickness on MagLIF fuel preheat by using the well-characterized OMEGA-EP laser varying the LEH foil thickness from $0.5 \mu\text{m}$ to $3 \mu\text{m}$. Two-dimensional (2D) HYDRA simulations accurately match the experimental observations for $0.5 \mu\text{m}$ and $1 \mu\text{m}$ thick foils but exhibit excessive propagation for $2 \mu\text{m}$ and $3 \mu\text{m}$ thick foils due to whole-beam self-focusing (referred to as self-focusing for the remainder of the paper), whereby the plasma density channel formed by the laser focuses the whole beam toward the axis. We note that the term self-focusing will not be used to refer to filamentary instabilities in this paper. Different assumptions and models are tested in the simulations to see their effect on the observed self-focusing. In some simulations, a tabulated thermal conductivity model generated with a combination of quantum molecular dynamics (QMD)¹⁴ and Lee–More–Desjarlais (LMD)¹⁵ calculations was used instead of an inline treatment that combines the Epperlein–Haines¹⁶ and Lee–More¹⁷ (EHLM) thermal conductivity models. The tabulated model reduced self-focusing in simulations of the $2 \mu\text{m}$ foil bringing them into agreement with the experiments; however, excessive self-focusing persisted for the $3 \mu\text{m}$ thick foils. In addition to the advanced conductivity models, Three-dimensional (3D) simulations were required to reduce self-focusing in the $3 \mu\text{m}$ foil case and bring the simulations into reasonable agreement with experiments. Based on the analysis presented, we believe the simulations broadly capture how much energy the laser deposits into the LEH foil and gas. The simulations and experimental results suggest that the amount of energy coupled into the Ar gas is highly correlated with the laser propagation length over the range of LEH foil thicknesses tested ($0.5\text{--}3 \mu\text{m}$). This is as expected from analytical Eqs. (2) and (3) that reasonably match the propagation depth as a function of coupled energy.

The paper proceeds as follows: Sec. II describes the experimental setup used. Section III describes comparisons between simulations and

experiments. Section IV describes the sensitivity of the simulations to different assumptions and models and how they affect the comparisons to experimental data. Section V describes the simulation energetics and compares experimental and simulated data to analytical theory and Sec. VI presents the conclusions.

II. EXPERIMENTAL SETUP AND ANALYSIS

The targets consisted of cylindrical tubes, shown in Fig. 1, that were 10 mm long, 4 mm outer diameter, and $100 \mu\text{m}$ wall thickness made from Rexolite with an LEH foil at one end and an end plug and target stalk at the other, as illustrated in Fig. 1(a). No external magnetic fields were applied to the targets unlike in integrated MagLIF experiments.¹⁰ The experiments were conducted across two campaigns with similar targets, as documented in Table I, with the primary variable being the LEH foil thickness.

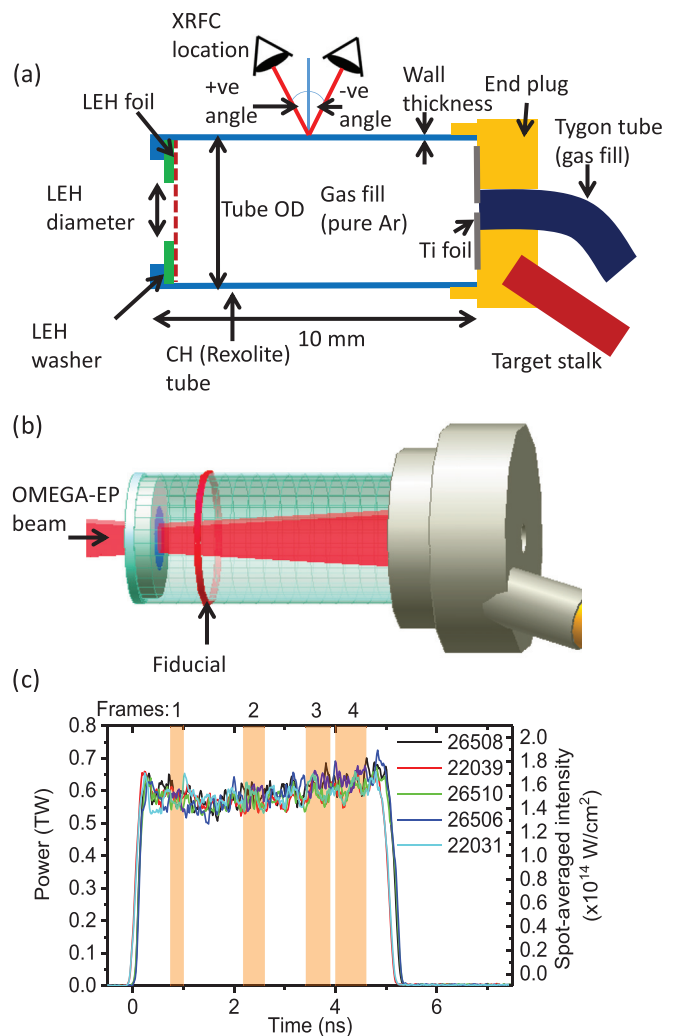


FIG. 1. (a) Drawing illustrating the typical target design and (b) VISRAD model of the target in the chamber including the OMEGA-EP heating beam and (c) laser pulses used in each shot described and the range of times over which each frame of x-ray framing camera data were taken.

TABLE I. Summary of experimental parameters for the targets used in this study.

Shot no.	Measured gas pressure (atm)	LEH diameter (mm)	LEH foil thickness/deflection (μm)	LEH dopant (outside)	LEH dopant (inside)	XRFC angle (deg)	Laser pulse shape/energy	XRFC frame duration (ns)
26508	1.27	1.6	0.51/300	None	20 nm Ti	-10	5 ns, 3058 J	0.2
22039	1.49	1.3	1/240	20 nm Ti	20 nm CaCl_2	10	5 ns, 2958 J	0.05
26510	1.31	1.6	2/80	None	20 nm Ti	-10	5 ns, 2975 J	0.2
22031	1.42	1.3	3/80	20 nm Ti	20 nm CaCl_2	10	5 ns, 2973 J	0.05
26506	1.29	1.6	3/80	None	20 nm Ti	-10	5 ns, 3000 J	0.2

All experiments used pure Ar gas fills, the pressure of which was continuously monitored up to shot time. The fill pressure varied slightly between shots at 1.27 and 1.49 atm (2.17–2.51 mg/cc) because the targets were filled ~ 1 hour before each shot and some leakage occurred. Ar was used instead of D_2 as the gas fill because it emits diagnosable K-shell line radiation ($h\nu \sim 3\text{--}4$ keV), where the tube wall is reasonably transparent (transmission $> 50\%$). Using Ar also reduces the pressure required to achieve a given electron density by a factor 8 due to the higher mean charge ($Z \sim 16$ vs 2 for D_2). This reduces the minimum LEH foil thickness that can be used to contain the gas fill without rupturing. We note that the unmagnetized Ar plasmas investigated here are not a completely ideal surrogate for the magnetized D_2 plasmas used in integrated MagLIF experiments. For the preheat conditions investigated in these experiments with Ar plasmas, effects such as hydrodynamic motion, filamentation, and self-focusing only play minor roles. In MagLIF experiments, these effects are expected to become more important. Nevertheless, we estimate that thermal conduction, radiative losses, and non-local electron transport are negligible during preheat for both cases. We have also previously established the ability to accurately simulate Ar-filled targets in HYDRA¹² which gives us confidence that the simulations can accurately model laser energy deposition into the gas in these simulations with minimal LPI.

Once the targets are pressurized, the LEH foil deforms to produce a bubble. The deflection of the bubble was only measured for the $0.5 \mu\text{m}$ thick foil ($300 \mu\text{m}$ deflection) and the $2 \mu\text{m}$ thick foil ($80 \mu\text{m}$ deflection) at shot pressures. In simulations, the deflection for the $3 \mu\text{m}$ thick foil was assumed to be the same as for $2 \mu\text{m}$ (likely a slight overestimate), and the $1 \mu\text{m}$ thick foil deflection was assumed to lie between the other thicknesses ($190 \mu\text{m}$ deflection). The effect of deflection on the simulations is explored further in Sec. IV. The simulations use a bubble shape given by: $y = dz(1 - r/r_{\text{washer}})^2$, where dz is the peak bubble height, with the simulation mesh conforming to the surface of the bubble. The details of the curvature was not observed to make a significant difference in these simulations. The thickness of the LEH foil is assumed to be constant across its surface and no thinning of the material due to deformation is assumed to occur. We note the relatively low pressures and small LEH diameters mean previous work measuring LEH foil deflections in MagLIF targets (where significantly higher pressures were used)⁵ is not applicable. In some experiments, 20 nm-thick Ti and CaCl_2 coatings were applied to the outside (laser-facing side) and inside (fuel-facing side) of the LEH foil as listed in Table I. These dopants were intended to allow for tracking of the foil material location spectroscopically, however no emission from the dopants was observed in these experiments. In simulations of a $1 \mu\text{m}$ LEH foil, 65 J more energy was absorbed when a 25 nm Ti coating was

included than without, or 2.5% of the 2.4 kJ incident energy. Because the coatings had little effect on the simulations and are challenging to model, they are not included in simulations going forward.

The experiments were driven with a single OMEGA-EP beam focused with an $f/6.5$ lens that passed through the LEH window and propagated down the axis of the target as shown in Fig. 1(b). The driving beam was spatially smoothed with a distributed phase plate (DPP) to give a reproducible 8th order super-Gaussian, $750 \mu\text{m}$ spot diameter containing 95% of the beam energy. All shots used square temporal pulse shapes with durations and energies listed in Table I and shown in Fig. 1(c).

The primary diagnostic in the experiments was an x-ray framing camera (XRFC) which takes four separate time-gated x-ray self-emission images of the plasma, which is dominated in the gas fill by emission from the Ar He- α and inter-combination lines at ~ 3.1 keV. The images were taken at approximately the same times in each experiment, with the range of times captured by each frame illustrated in Fig. 1(c). An example of the XRFC target view is shown in Fig. 1(b). The angle that the XRFC views the target, illustrated in Fig. 1(a) and listed in Table I, determines the precise field of view of the diagnostic. In some experiments, a Cu fiducial strip was glued around the target circumference at a measured distance from the LEH foil to enable better registration of the images. The strip is observed clearly in images blocking emission as seen in Fig. 2. In experiments where a fiducial was fielded, the LEH foil can be determined to ± 0.05 mm, while in targets without the fiducial the LEH foil location is inferred by relating emission features to the target design with an accuracy of ± 0.2 mm.

Based on analysis of previous experiments at higher laser intensities,¹² we do not believe that there were significant laser plasma instabilities present in the experiments. Therefore, no quantitative measurements of stimulated Brillouin scattering (SBS) were made; however hard x-ray detectors were fielded in the experiments that detect signatures from stimulated Raman scattering (SRS) and two-plasmon decay (TPD). Neither of these diagnostics recorded a signal strong enough to measure on these shots.

III. EXPERIMENTAL RESULTS AND COMPARISONS TO SIMULATIONS

Experimental and simulated XRFC images taken for five shots where the LEH foil thickness was varied between $0.5 \mu\text{m}$ and $3 \mu\text{m}$ are shown in Fig. 2. Four XRFC images were taken in each experiment that span the duration of the pulse shape at $\sim 0.9, 2.3, 3.5,$ and 4.1 ns after the start of the laser pulse, although slight variations in timing between shots did occur. The frame duration in each experiment is listed in Table I. The experimental frames have been stretched

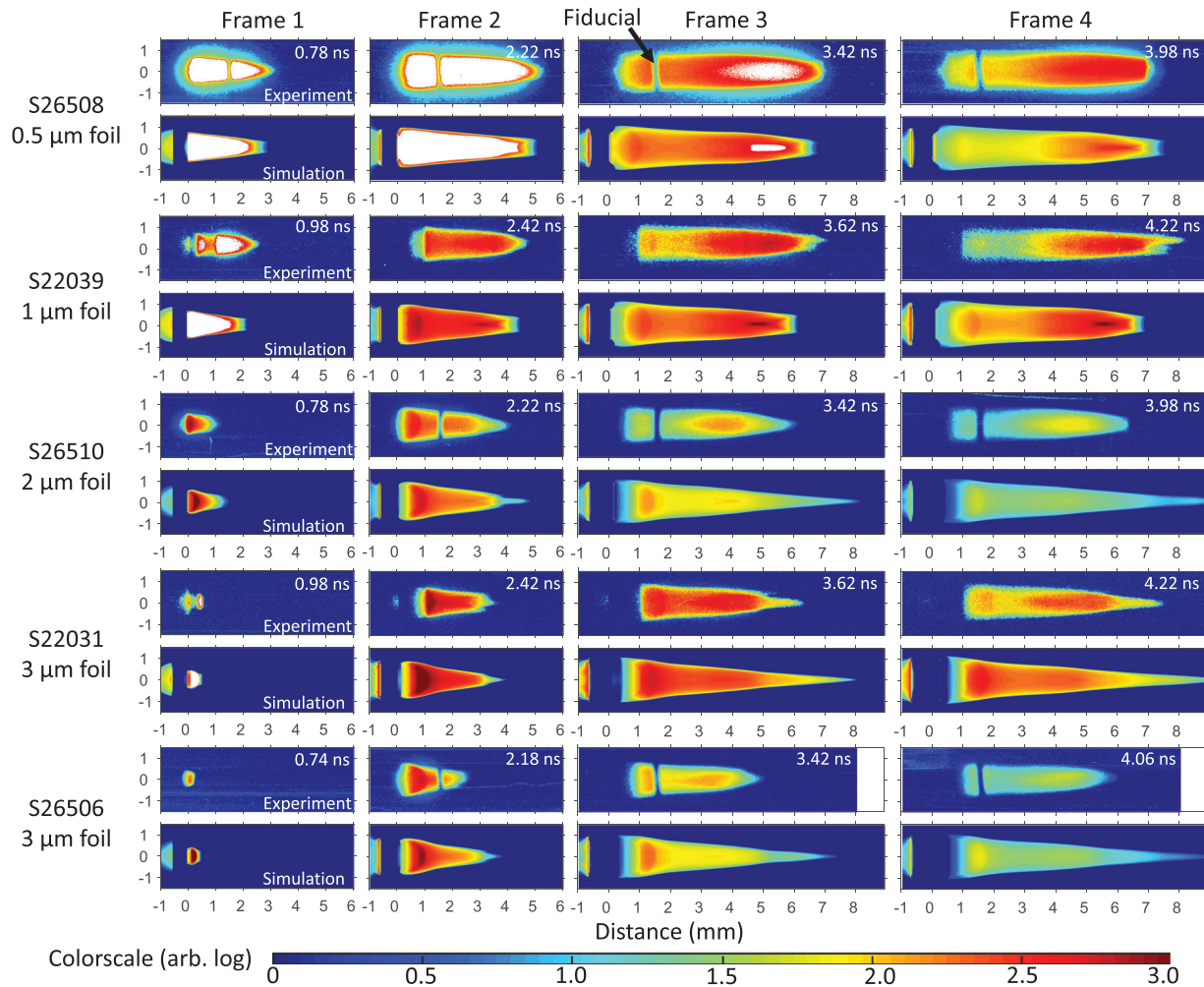


FIG. 2. Experimental and simulated XRF images for experiments with different LEH foil thicknesses. The vertical band present at $x \sim 1.5$ mm in some images is due to a Ti strip fiducial. The laser enters from the left in all images and the LEH foil location is at 0 mm. The simulations show good agreement with experiments for 0.5 μm and 1 μm thick foils but show excessive propagation in later frames due to self-focusing for 2 μm and 3 μm thick foils.

horizontally by 1.5% to account for the 10° XRF viewing angle listed in Table I. For the 50 ps-long frame duration images, a single simulation image was generated at the end of the XRF time. For 200 ps-long frame duration images, four simulation images in 50 ps time increments spanning the integration time were generated and summed. This allowed the motion blurring that occurs over the 200 ps frame duration to be captured. The experimental and simulated images are presented on a common logarithmic scale spanning three decades of intensity. The experimental data are multiplied by a factor to give consistent signal levels between simulations and the data for a single shot, and that factor was kept constant for that particular camera. For example, the normalization factors for s26510 were also used in s26508 and s26506 and the normalization factors for s22039 were also used in s22031. Based on signal differences between co-timed frames recorded on experiments that used the same cameras, we estimate that there is an approximate factor 2 relative uncertainty in the signal levels between frames in regions where the detector is not

saturated and we do not anticipate significant shot-to-shot variations in the sensitivity beyond this. However, this does not significantly impact the propagation depth comparisons as discussed later in this section. In some images, for example in shot 26508, a low intensity halo surrounds the most intense portions of the emission. This is evidence of detector saturation and the signal levels do not reflect the signal intensity close to these regions. The approximate signal levels that correspond to this saturation were calculated and the data are colored white in regions where this signal level is exceeded in the experiments and simulations.

The experiments were modeled using the radiation-hydrodynamics (RHD) code HYDRA that is used extensively to model and design MagLIF experiments¹⁸ and past OMEGA-EP experiments^{12,19} as discussed. The laser package employs a ray tracing algorithm and accounts for inverse bremsstrahlung absorption, refraction, and ponderomotive effects, but not LPI processes such as SRS, TPD or SBS. However, as discussed above, these processes are not expected to

play a significant role in the laser-plasma coupling and energy balance. To model inverse bremsstrahlung, we did not include the Langdon effect²⁰ which can reduce absorption by the plasma for large Z .²¹ The simulations presented in this section assume 2D axisymmetry, use an electron thermal flux limiter of $f=0.1$, multi-group radiation transport, non-local thermodynamic equilibrium (non-LTE) opacities,²² and the EHLM transport coefficients for conduction.¹⁶ Radiation groups span 1 eV–100 keV but are focused in the 3–4 keV range. Experimental targets are modeled from ambient conditions. The axial extent of the initial zones was 50 nm in the LEH foil (sufficient for multiple zones over the foil thickness) and 25 μm in the gas. The initial radial extent of the zones ranged from 6 to 8 μm with finer zoning near the center. Tabular EOS are used for both argon and the polyimide.

HYDRA is also augmented with a resistive MHD package that includes a generalized Ohm's Law that neglects displacement current. For the best surrogacy with previous work, this package was not used for the 2D simulations. For the 3D simulations presented in Sec. IV, the MHD package was enabled to examine the effect of self-generated magnetic fields, using the full tensor form of the Epperlien–Haines transport coefficients. Important components included in the induction equation that describes the evolution of magnetic fields in the generalized Ohm's law are shown in Eq. (1) below in the form of Braginskii and Epperlien–Haines

$$\begin{aligned} \frac{\partial \mathbf{B}}{\partial t} \sim & \nabla \times \mathbf{v} \times \mathbf{B} - c \nabla \times \left(\frac{\alpha_{\perp} \mathbf{J}}{(en_e)^2} \right) + c \nabla \times \left\{ \frac{\nabla p_e}{en_e} \right\} + c \nabla \\ & \times \left[\frac{\beta_{\wedge}}{|B|en_e} \mathbf{B} \times \nabla T_e \right], \end{aligned} \quad (1)$$

where \mathbf{v} is the fluid velocity, \mathbf{B} is the magnetic field, \mathbf{J} is the current density, n_e and p_e are the electron density and pressure, α_{\perp} is the electric resistivity coefficient and β_{\wedge} is the Nernst coefficient. The terms from left to right are: fluid advection, resistive diffusion, Biermann battery ($\nabla n_e \times \nabla T_e$ for an ideal gas), and the Nernst advection term. Self-generated magnetic fields are sourced from the thermal terms (not shown) and the Biermann term in the generalized Ohm's law which can then impact thermal conduction. Frozen-in and Nernst advection are the dominant terms responsible for redistributing the field (though we include resistive diffusion). Nernst (β_{\wedge}) is large when the plasma is marginally magnetized and decreases with increasing magnetization. The Hall term in the induction equation was included in one simulation and was found to produce negligible impact. In Hydra including the Hall effect add substantially to the simulation runtime so it was neglected for the majority of the MHD simulations. The effect of each of these assumptions will be discussed further in Sec. IV.

Simulations were post-processed using the Spect3D code^{23,24} (utilizing tabulated NLTE opacities generated by the related Propaceos code) to generate the XRFC images filtered through the 100 μm outer wall of the target. The XRFC images are analyzed in a similar way to that outlined in Harvey-Thompson *et al.*¹¹ Lineouts of the images and simulations, shown in Fig. 3, were taken at $r=0$ averaged over the central $\pm 0.2\text{mm}$. The shape and magnitude of the simulated and experimental lineouts is generally consistent away from the LEH foil. The viewing angle that the XRFC observes the target, described in

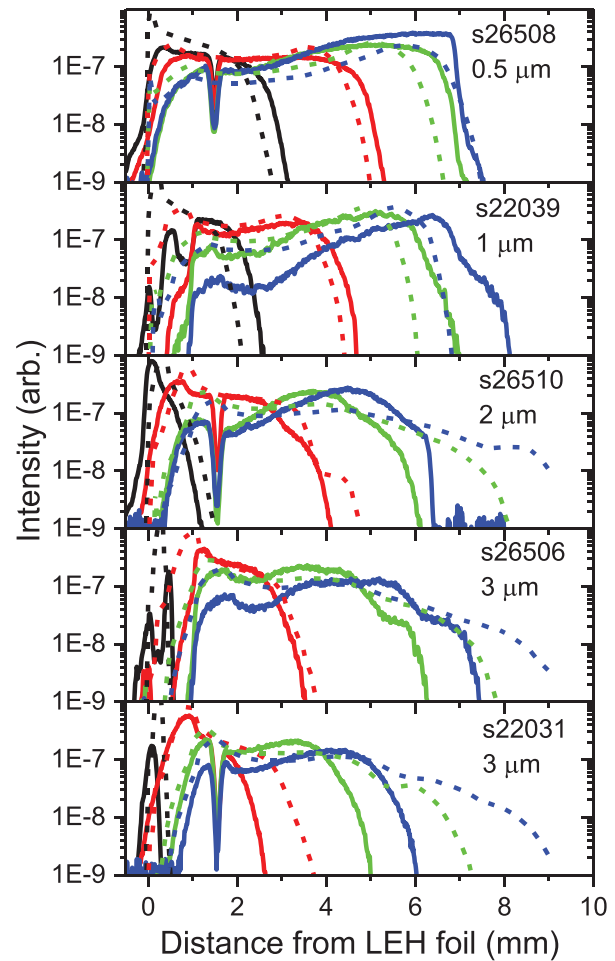


FIG. 3. Axial lineouts over the central $\pm 0.2\text{mm}$ for (solid) experimental and (dashed) simulated XRFC images shown in Fig. 2. The colors correspond to different frames in Fig. 2 as follows: Frame 1 (black), frame 2 (red), frame 3 (green), and frame 4 (blue).

Sec. II, partially obscures the region close to the LEH foil (at $x \leq 1\text{mm}$) in some experiments complicating comparisons in that region.

The lineouts in Fig. 3 are used to assess the axial extent of the emission (the propagation depth) by locating where the axial lineout intensities drop below values of 1.25×10^{-8} and 5×10^{-8} that define the upper and lower bounds for the propagation length. This range accounts for the approximate factor 2 uncertainty in signal levels and also serves to highlight the extended emission regions in the data described later. The propagation depths obtained from this analysis are shown in Fig. 4 for the 0.5 μm , 1 μm , and 2 μm LEH foil experiments. The vertical error bars in Fig. 4 combine the distance error associated with this range in intensities with the uncertainty in LEH position and the error in the magnification of the image (2%). The error in energy delivered represents the range of energies delivered over the duration of each frame. As described in Harvey-Thompson *et al.*,¹² the propagation distance as assessed by the extent of the observed emission here does not represent the full energy deposition length, which typically extends a few mm beyond that observed.

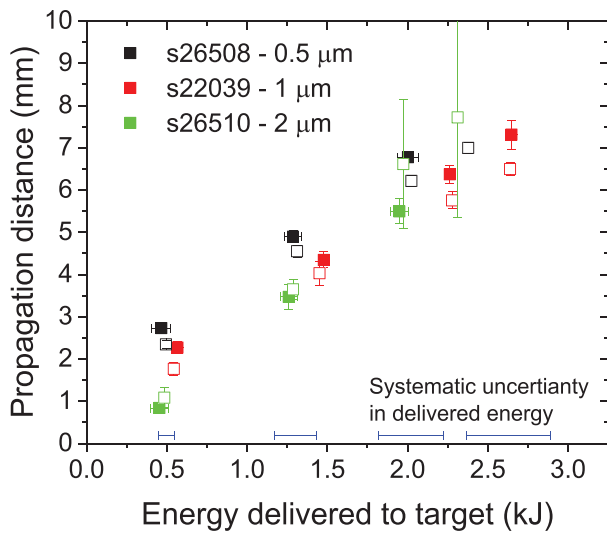


FIG. 4. Plot of propagation distance vs delivered energy assessed using experimental (solid square) and simulated (open square) lineouts shown in Fig. 3. At late times, simulations of the 2 μm foil case show excessive propagation due to self-focusing which manifests as a larger mean propagation and vertical error bars in the plot. The data for the fourth frame is not included for the 0.5 μm and 2 μm foil cases because the laser has reached the end of the target by this time.

As shown in Figs. 3 and 4, the simulations under-predict the propagation for the 0.5 μm experiments by $\sim 10\%$ and the 1 μm thick foil experiments by between 10 and 20%—greater than the propagation uncertainty of less than $\pm 5\%$. This discrepancy may be partially explained by a $\pm 10\%$ systematic uncertainty in the energy delivered to the target, as represented by the blue error bars in Fig. 4, but does not fully account for the discrepancies at all times. The uncertainty in the energy delivered is calculated from uncertainties in the measurement taken at the frequency conversion crystals and in the transmission into the target chamber. For the 2 μm foil experiment, the simulations closely match the first two frames but then start to dramatically over-predict the penetration depth in the final two frames. The large error bars in propagation distance arise because the emission at the leading edge of the propagation drops gradually in this region as opposed to decreasing more rapidly in earlier frames, as can be seen in the lineouts in Fig. 3 and the images in Fig. 2. Similar behavior is seen in simulations of the 3 μm thick LEH foil experiments. A comparison of the propagation for these experiments is shown in Fig. 5.

The extended emission observed in the simulations of 2 μm and 3 μm foil experiments is caused by the beam undergoing self-focusing that is initially seeded by the density gradients near the LEH foil region. Figure 6 shows an intensity map taken from simulations of the third frame for the 0.5 μm foil and 3 μm foil cases at ~ 3.6 ns (approximately 2 kJ delivered). LEH foil material refracts the beam in both cases resulting in a less intense region on axis close to the foil location but in the 3 μm case another channel forms in the plasma further from the LEH that focuses the beam onto the axis. This is generally not observed in the experimental lineouts, however, in frames 3 and 4 of shot s22031 the emission front appears to show an extended emission feature developing.

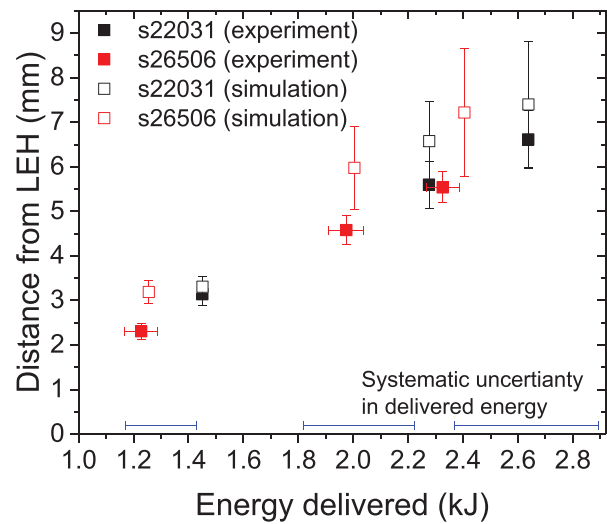


FIG. 5. Plot of propagation distance vs delivered energy for the experiments and simulations of 3 μm thick LEH foils. The distance for the first frame is not included for either shot because emission remains very close to the LEH foil location at this time.

IV. SIMULATION SENSITIVITIES

The simulations in Sec. III exhibit some differences with the experimental data. For the 0.5 μm and 1 μm foils, the simulated propagation distances slightly lag the experimental measurements while for

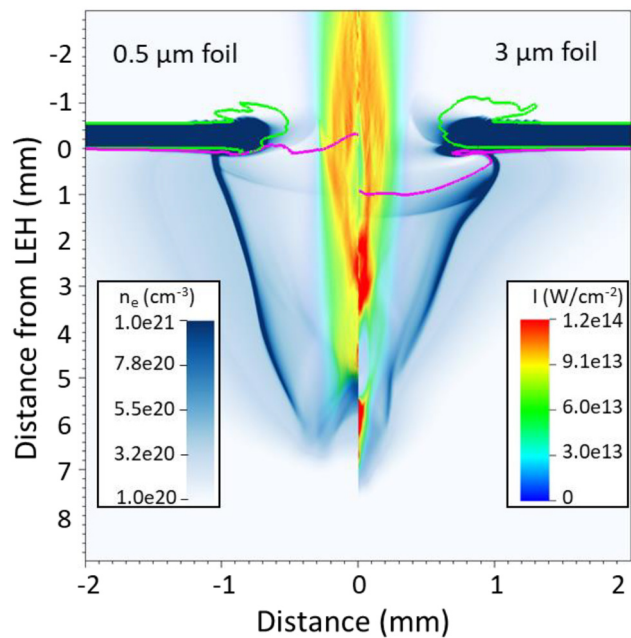


FIG. 6. Intensity map taken from HYDRA simulations of the 0.5 μm (left) and 3 μm thick LEH foil case (right) at 3.6 ns. The red lines indicate the boundary where LEH foil material is present and the green lines indicate where washer material is present. The 3 μm thick LEH foil case shows a region of enhanced intensity deep into the gas due to self-focusing.

the 2 μm and 3 μm LEH foils, the simulations exhibit self-focusing within the targets resulting in increased propagation depth compared to the experiments. In this section some of the simulation sensitivities that may account for these discrepancies are discussed and analyzed.

Figure 7 shows experimental and simulated propagation distances for the 0.5 μm foil case with and without the assumption of Local Thermodynamic Equilibrium (LTE) for radiation transport and for different flux limiters where LTE is assumed. For this comparison, the mean simulated propagation is plotted every 200 ps so different models can be distinguished. The simulations show little dependence on the flux limiter and a slight decrease in propagation depth when LTE is assumed due to the plasma channel being slightly wider, putting the simulations further from the experimental results. The lack of dependence on the flux limiter in similar experiments was reported previously.¹² Similar simulations varying the flux limiter for the 2 μm and 3 μm cases also show no impact on self-focusing.

Another parameter that might be reasonably expected to affect self-focusing and that has significant uncertainty is the initial deflection of the LEH foil in the experiments. As described in Sec. II, the deflection of the LEH foil is approximately known based on previous testing, however the deflection was mistakenly not measured after target assembly or during the experiments for the 1 μm and 3 μm foil cases. Figure 8 shows the propagation depth as a function of energy delivered for the 0.5 μm and 3 μm thick foil cases where different LEH foil deflections are assumed. The 3 μm foil target used in s26508 was pressurized to ~ 4 atm in pre-shot testing, which may have stretched the foil inelastically and increased the deflection height in the experiment. Using a 300 μm deflection for the 3 μm thick foil case reduces the propagation depth by ~ 300 – 600 μm at most times but does not prevent the self-focusing observed in the simulations. This is likely an overestimate of the LEH deflection even given the testing to higher pressures. Using an 80 μm deflection for the 0.5 μm thick foil case increases the propagation depth by ~ 300 μm from the baseline 300 μm deflection case, bringing the simulated propagation depth

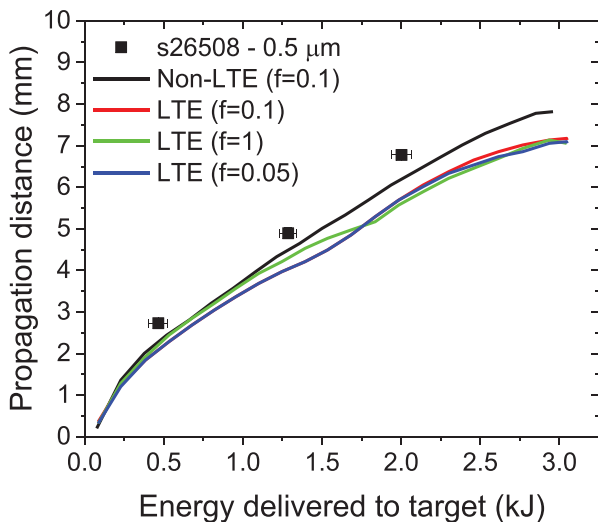


FIG. 7. Plot of propagation depth vs delivered energy for the 0.5 μm thick foil case under different assumptions for local thermodynamic equilibrium and for different values of the flux limiter, f .

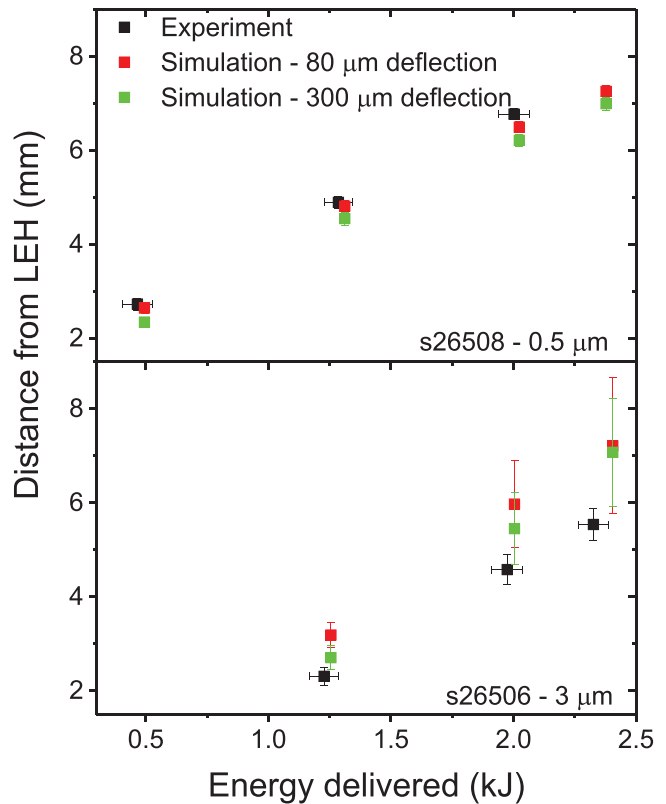


FIG. 8. Experimental and simulated propagation distances for (top) the 0.5 μm LEH foil and (bottom) the 3 μm LEH foil cases comparing different values for the LEH foil deflection. The simulated propagation values for the 3 μm foil cases are represented by two points showing the maximum and minimum propagation.

closer to the experimental values. However, this is likely an underestimate of the foil deflection. Overall, the uncertainty in the LEH foil deflection alone does not explain differences in the experimental and simulated propagation lengths and does not strongly affect the self-focusing in simulations.

The simulations in Sec. III used an inline treatment for thermal conductivity for the argon and polyimide window that uses Epperlein-Haines coefficients with Lee-More degeneracy conditions. More sophisticated models using QMD and LMD calculations exist for polycarbonate ($\text{C}_{15}\text{H}_{16}\text{O}_2$)²³ that can be tabulated and used in simulations for the LEH foil material. At present, no such tabulated conductivities are available for polyimide. Relative to EHLM, the tabulated thermal conductivity for polycarbonate is less conductive under ambient conditions, becomes more conductive for temperatures between a few eV through ~ 40 eV at densities near solid, and is more conductive again at temperatures > 200 eV. At lower densities (around 1×10^{-3} g/cc) the tabulated and inline conductivities are within a few percent beyond 50 eV. The choice of conductivity model therefore has the largest impact early on, when the density of the window material is still high though it is difficult to determine where in phase space may be most responsible for our observations. The choice of polycarbonate is not necessarily intended to accurately reflect the conductivity of polyimide whose composition differs and includes nitrogen. Rather,

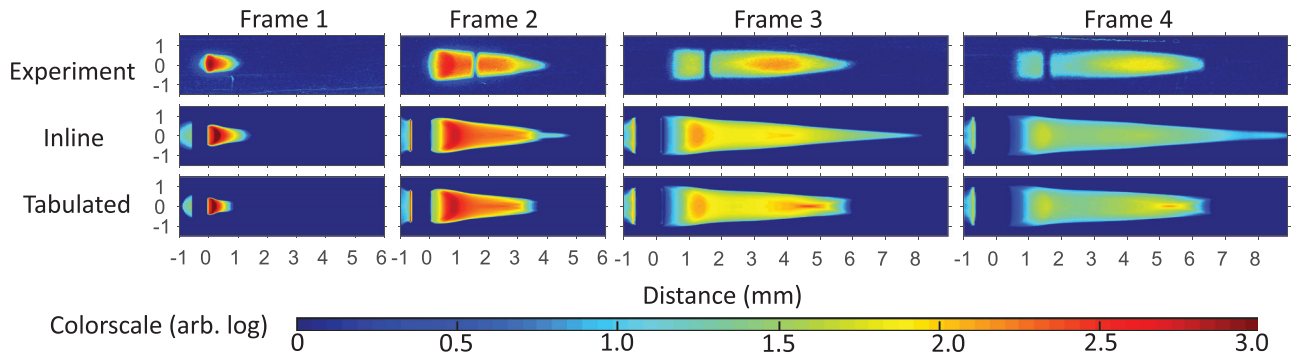


FIG. 9. Experimental and simulated XRF images for the 2 μm thick foil case comparing tabulated (polycarbonate) and in-line thermal conductivity models for the polyimide foil. Using a tabulated model significantly reduces self-focusing bringing the simulation into better agreement with experiments.

polycarbonate is chosen as a plastic compound with an available conductivity table that will demonstrate the sensitivity of the simulations to changes in the thermal conductivity of the LEH foil material. Simulations using a polycarbonate EOS show similar qualitative trends as we show next.

Figure 9 shows the effect of using the tabulated polycarbonate thermal conductivities in simulations of the 2 μm LEH foil experiment on the simulated XRF images. The use of a tabulated thermal conductivity model essentially eliminates self-focusing, reducing the extended emission in the simulated XRF images. This behavior occurs because of very subtle changes to the density distribution in the LEH and gas plasmas resulting in slight changes in the direction that rays travel as they enter the gas. There is very little difference in the amount of energy coupled to the LEH foil material between the conductivity models ($<3\text{ J}$ for the 2 μm foil case). This behavior highlights how sensitive whole-beam self-focusing can be to subtle changes in the plasma density profiles.

Figure 10 shows a comparison of the propagation distance for the 2 μm and 3 μm thick LEH foil cases for tabulated and in-line thermal conductivities. By eliminating the self-focusing in simulations of the 2 μm thick LEH foil case, the tabulated conductivity model brings the simulations into good agreement with experiments. However, the simulations for the 3 μm thick LEH foil case still exhibit strong self-focusing and increased propagation when a tabulated thermal conductivity is used. The different thermal conductivity models were also found to have little effect for the 0.5 and 1 μm thick LEH foil cases.

The persistence of excessive propagation due to self-focusing in 2D simulations of the 3 μm -thick LEH foil experiments may be due to several reasons: (1) the simulations did not include MHD effects and (2) the 2D simulations produce an azimuthally symmetric density channel that effectively self-focuses the rays that are forced to cross the axis of the simulation. Adding the MHD package into the 2D simulations did not reduce the discrepancies between simulations and experiments. This motivates 3D simulations where azimuthal symmetry is not enforced and self-focused rays have a greater freedom to traverse the plasma, potentially reducing the impact of self-focusing on the propagation depth. Figure 11 shows synthetic XRF images from 3D simulations with and without the inclusion of MHD terms in Ohm’s law. Generally, 3D simulations are computationally expensive and may require assumptions that simplify the physics to reduce the computational cost. The 3D simulations here assume LTE opacities.

The 3D simulations also used coarser zoning with the initial axial extent being 125 nm in the LEH foil and 50 μm in the gas and the radial extent being 25 μm everywhere. However, all other simulation inputs such as the laser spot and EOS models are identical to the 2D model. 3D simulations reduce the on-axis focusing by allowing the beam to breakup in the azimuthal direction as well. Generally, the 3D simulations still show a high degree of axisymmetry (as do the experiments), but near the end of propagation the laser tends to split into three individual beamlets with MHD (two without MHD) that is not allowed in 2D.

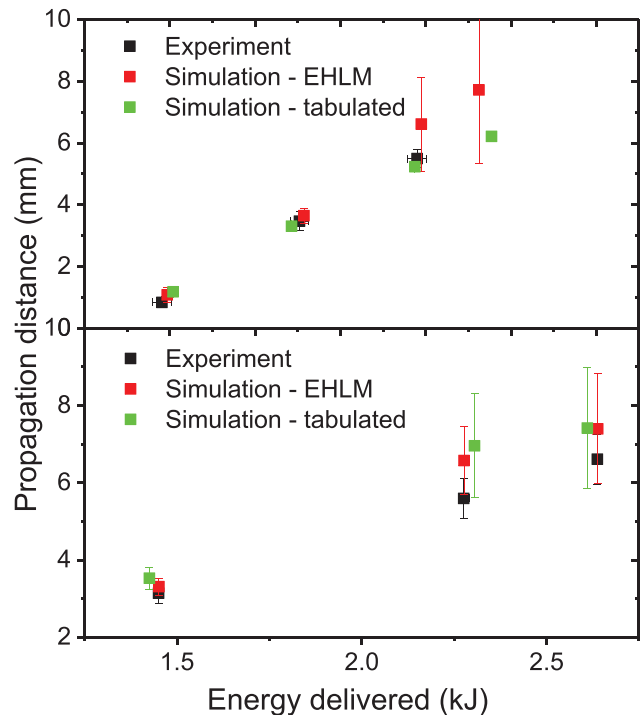


FIG. 10. Experimental and simulated propagation for (top) the 2 μm LEH foil and (bottom) the 3 μm LEH foil cases comparing simulations using the EHLM and tabulated thermal conductivities for the LEH foil material.

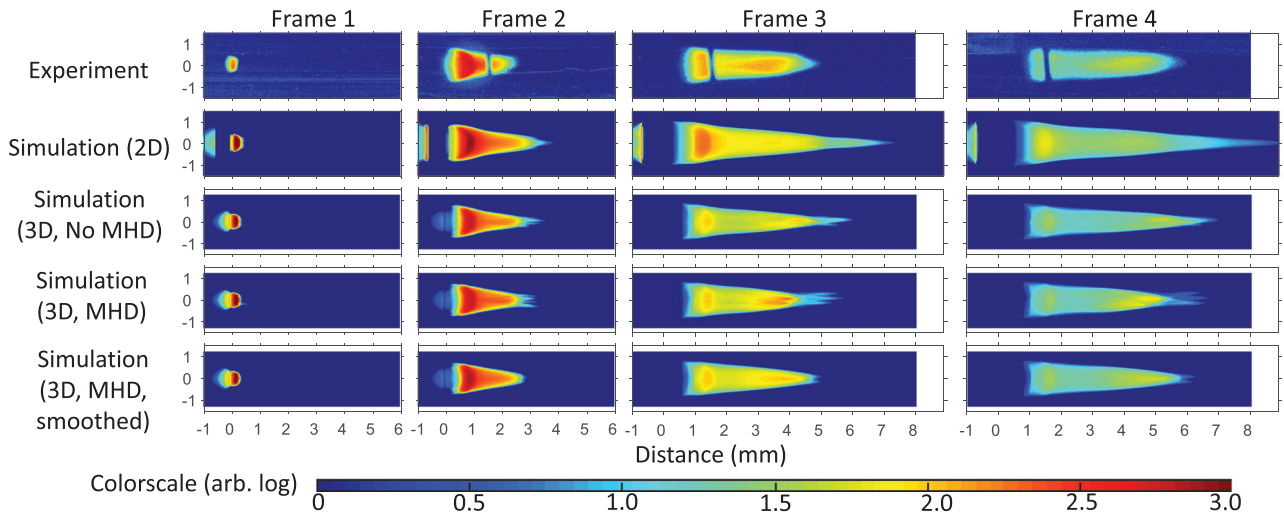


FIG. 11. Experimental and simulated XRF images for s26506 ($3\ \mu\text{m}$ thick foil case) comparing 2D and 3D simulations with different assumptions. The 3D simulations exhibit significantly less self-focusing and show propagation depths more similar to experiments.

With MHD, the Biermann battery term generates magnetic fields on the edges of the emitting plasma regions. The strongest fields reach approximately 10 T near the window/gas interface (the strongest emitting feature of frame 2) as shown in Fig. 12, sufficient to reduce perpendicular conduction by 50%–60%. This reduces energy losses from the LEH foil material and over the course of the simulation 100 J less is coupled to the window material compared with the no-MHD case. The inclusion of MHD also affects how the beam is refracted as it passes through the foil material resulting in a slightly wider emission profile with less self-focusing.

The 3D simulations both exhibit filaments at the leading edge of the propagation that are not observed in experiments. This may be due to the finite number of rays that can be included without being too computationally expensive. To overcome this limitation and reduce statistical noise from the laser package, smearing of the laser deposition can be applied where the energy in each “ray” is deposited over a number of zones. The results from a simulation including this smearing is shown in Fig. 11. The smearing eliminates the filaments present at the leading edge in the other 3D simulations bringing it in

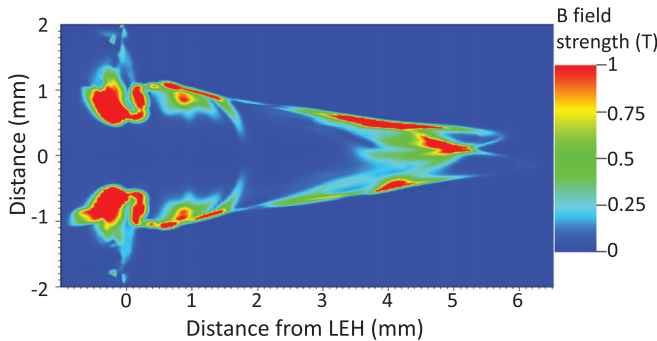


FIG. 12. Simulated magnetic field strength generated by the Biermann battery term taken from frame 3 of the 3D, MHD, unsmoothed simulation shown in Fig. 11.

closer agreement with experiments. This smearing was found to have a negligible impact on 2D simulations since there is almost no limitation to the number of rays that can be used since the NLTE package is the most computationally expensive.

The synthetic XRF images in Fig. 11 show that the self-focusing and excessive propagation exhibited in the 2D simulations is greatly reduced in 3D. The propagation for each case is shown in Fig. 13 using the same metrics as described in Sec. III. The analysis highlights that 3D simulations significantly reduce the self-focusing and excessive propagation observed in 2D simulations and are generally closer to the experimental values. This is primarily because in 3D, unlike in 2D,

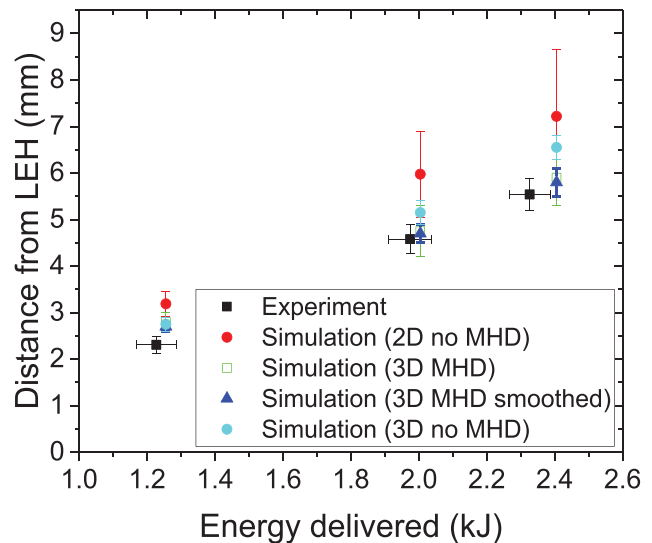


FIG. 13. Experimental and simulated propagation for s26506 ($3\ \mu\text{m}$ thick LEH foil case) comparing 2D and 3D simulations under different assumptions. The 2D simulations are described in Sec. III.

rays that self-focus in the plasma channel do not have to traverse the exact center of the plasma which limits the intensity enhancement of this effect. In 3D, the addition of MHD terms does make difference to the propagation depth with simulations that include MHD being closer to the experiments. We note that applying the effects of self-generated magnetic fields to simulations of thinner foils has very little effect. Finally, both of the “unsmoothed” 3D simulations see more structure within the emission, particularly at the leading edge, due to beam filamentation than is seen in experiments. The 3D, smoothed simulation comes closest overall to matching experiments both in terms of propagation distance and the qualitative emission profile shown in Fig. 11, although the differences between the 3D simulations are generally within error bars.

V. SIMULATION ENERGETICS

To be effective, MagLIF preheat must deposit energy within the ~ 10 mm tall imploding portion of the target without introducing significant mix which integrated experiments suggest can be sourced from the LEH foil and top and bottom cushions.^{6,25} In particular, mix may become more severe if energy is deposited beyond the imploding region where there is a beryllium “bottom cushion” feature that effectively narrows the inner diameter of the target to 3 mm (from 4.65 mm) and is at risk of being directly illuminated by the laser. For MagLIF preheat, it is therefore important to determine what factors affect the energy deposited into the fuel within a given propagation length.

As shown in Secs. III and IV, HYDRA simulations are able to reproduce the propagation depths observed in experiments using 0.5–3 μm thick LEH foils reasonably well, depending on the assumptions made. The most impactful assumptions tested were the dimensionality (2D vs 3D), the thermal conductivity model of the LEH foil material (EHLM vs tabulated), and how much smearing is applied to the simulated laser profile. All of these assumptions can significantly impact the self-focusing and simulated propagation distance, but do not have a large effect on amount of energy coupled into the foil material or gas. For example, for the 3 μm thick foils, the 2D simulations with different assumptions deliver energies that are within a few percent at the end of the laser pulse. The largest difference is between the 3D and 2D simulations with the largest total difference being between the 3D, with MHD unsmoothed and 2D with tabulated thermal conductivities that deposited 2.0 kJ and 1.7 kJ, respectively, at the end of the laser pulse. However, the difference in deposited energy between the different models is less than 10% at the experimental frame times. Based on this, we hypothesize that disagreement between experiments and simulations for the 3 μm thick LEH foils are not the result of gross differences in how much energy is deposited into the LEH foil and Ar gas but rather the distribution of energy in the gas. This assumption will be made for the remainder of this section.

Figure 14 shows the laser energy and power deposited into the LEH foil material and Ar gas for the different thickness foils taken from the simulations described in Sec. III. At early times in the simulations, energy is almost exclusively coupled into the LEH foil material until it is heated and rarefied sufficiently for it to become transparent to the laser. The energy invested for this to happen is dependent upon the foil thickness with the 0.5 μm foil requiring ~ 65 J and the 3 μm foil requiring ~ 556 J before >10 J of energy is coupled into the gas. The energy invested per micrometer of foil material before it becomes

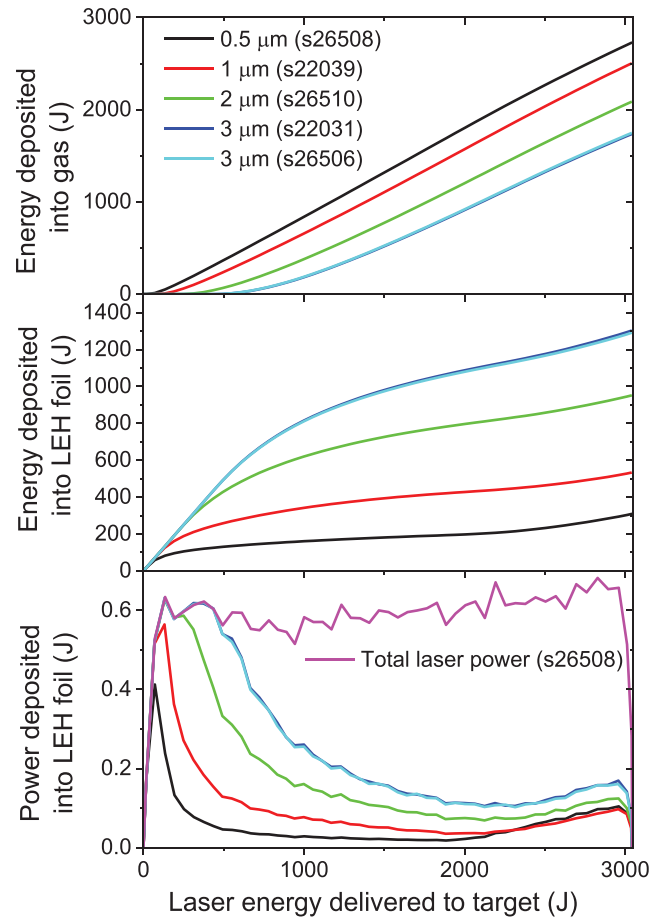


FIG. 14. Simulated values for the energy and power coupled into the LEH foil material and gas for the different LEH foil thickness cases taken from the 2D simulations described in Sec. III.

transparent increases slightly, with thickness requiring 130 J/ μm , 140 J/ μm , 162 J/ μm , and 185 J/ μm for the 0.5 μm , 1 μm , 2 μm , and 3 μm thick foil cases, respectively. After this occurs, energy continues to be coupled into the foil material primarily to maintain its temperature and counteract radiative cooling. By the time 2 kJ of laser energy has been delivered (~ 3.5 ns into the laser pulse corresponding to frame 3 in the XRFC data), 396 J/ μm (198 J), 427 J/ μm (427 J), 398 J/ μm (796 J), and 360 J/ μm (1080 J) have been deposited into the 0.5 μm , 1 μm , 2 μm , and 3 μm thick LEH foils, respectively. At this time, there is a gradual trend toward less energy per micrometer deposited for thicker foils, although the 0.5 μm thick foil breaks this trend. This may be because the entirety of the foil material is pushed up and out of the target rather than inwards as for the 1–3 μm thick foils as shown in Fig. 6. At later times, after ~ 2500 J of energy has been delivered to the target, the rate of energy coupled into the foil material begins to increase again, particularly for the 0.5 μm foil case. This is a result of the ablation of the washer material driving a shock inward radially that compresses the ablating window material, which reduces the mean free path of the laser passing through it.

Under the assumption that the simulations are correctly capturing the gross energetics in the experiments, the energy deposited into the gas (from simulations) as a function of the propagation length observed in the experiments can be assessed as shown in Fig. 15. The data suggest that for the range of LEH foil thicknesses tested in these experiments the observed emission length is primarily dependent upon the energy deposited into the gas and is not directly sensitive to the LEH foil thickness.

Figure 15 also shows the propagation distance as a function of laser energy in the gas, as calculated by an analytical model of inverse bremsstrahlung absorption in a gas.⁴ The model assumes a stationary plasma with constant electron density that is initially cold and excludes hydrodynamic motion, heat conduction and any LPI. According to this model the distance, z_* , at which a minimum energy density, \mathcal{E}_{min} , is reached for a given laser energy, E_{laser} , delivered in a cross-sectional area σ is given by

$$z_*(E_{laser}) = \frac{2}{3\tilde{\kappa}} \left[\left(\frac{5\tilde{\kappa}}{2\sigma} E_{laser} \right)^{3/2} - \mathcal{E}_{min}^3 \right], \quad (2)$$

where $\tilde{\kappa}$ is a modified absorption coefficient given by

$$\tilde{\kappa} \doteq \frac{4\sqrt{2}\pi n_i Z^2 e^4 \ln \Lambda}{(4\pi\epsilon_0)^2 3\sqrt{m_e c}} \left[\frac{3n_i(1+Z)}{2} \right]^{3/2} \frac{\omega_p^2}{\omega^2} \left(1 - \frac{\omega_p^2}{\omega^2} \right)^{-1/2}. \quad (3)$$

A detailed re-derivation of these equations is given in the Appendix. Equation (2) suggests that the distance as a function of laser energy, $z_*(E_{laser})$, is independent of the time history of the laser power, which agrees with the results in Fig. 15. The propagation distance vs energy in the gas from this model is plotted in Fig. 15 for the highest and lowest gas pressures measured in experiments: 1.27 and 1.49 atm ($n_e = 5.1\text{--}6.0 \times 10^{20} \text{ cm}^{-3}$). The curves were calculated assuming a beam area of $1.8 \times 10^{-7} \text{ m}^2$ that contains 50% of the energy, which is

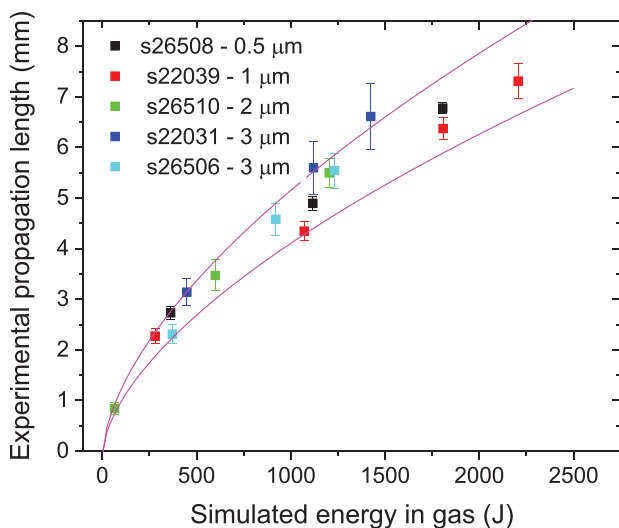


FIG. 15. A plot of the experimentally measured propagation distance vs the simulated energy deposited into the gas (taken from Fig. 14) at that time. The pink lines are the results from the analytical model of inverse Bremsstrahlung absorption given in Eq. (2) for 1.27 and 1.49 atm fill pressures.

as measured at best focus for the DPP optic used. Based on calculations using the model PrismSpect,²⁶ the ionization, Z , of the Ar plasma ranges from 15.89 to 16.29 for 500–1500 eV and is assumed to be 16 (He-like) in the calculation. The LEH foil is not modeled in this approach. The minimum energy density is chosen to be that where the temperature exceeds 500 eV, approximately the temperature threshold for observing emission in the simulations. Using these parameters, this simple model reasonably captures the propagation as a function of energy observed in the experiments.

This analysis suggests that, for these experiments that utilized an AR gas-fill, physics that would lead to deviations from the analytic model, such as hydrodynamic motion of the gas as it is heated, filamentation of the beam, and LPI, do not dramatically affect the energy deposition. We note that while this appears to be the case over the parameter range tested, it will not necessarily continue to hold for thicker LEH foils. Furthermore, using thinner LEH foils has other benefits such as absorbing less laser energy meaning more laser energy is available to be deposited into the fuel, which is currently a limitation in MagLIF experiments.¹¹ Thicker LEH foils can also lead to greater LEH foil mix, which is known to be present in MagLIF experiments.^{6,25}

VI. CONCLUSIONS

The most important parameters when designing effective MagLIF laser preheat are the specific energy coupled into the fuel (i.e., energy per mass), the propagation length of the laser, and the amount of mix introduced. Regarding energy deposition, the results in Fig. 15 suggest that the energy that can be coupled within a given propagation distance is insensitive to the LEH foil thickness for the parameter range tested. This is also well described by analytic theory. Therefore, using thinner LEH foils will not necessarily increase the amount of laser energy that can be coupled within a MagLIF target. However, a key assumption in the analytic theory required for this behavior is that there is no hydrodynamic motion of the gas as it is being heated which would tend to form a low-density channel. This may be approximately true for the experiments presented here where a limited length of gas (~ 8 mm) is observed to be heated for a short amount of time (~ 3 ns) and where the range of LEH foil thicknesses tested did not dramatically affect the peak laser power deposited into the gas. However, we may expect this assumption to no longer be valid for lighter gases (e.g., D_2) where more hydrodynamic motion can occur, or for thicker LEH foils that dramatically reduce the peak power delivered to the gas, or when the laser and plasma conditions are such that LPI becomes significant as in some MagLIF experiments.^{5,27}

The analysis presented in this paper shows that 2D Hydra simulations are generally able to capture the length over which laser energy is deposited into MagLIF-like targets provided thin LEH foils ($< 2 \mu\text{m}$ thick in these experiments) are used. For thicker LEH foils, the simulations are more prone to excessive propagation driven by self-focusing along the axis than is observed in experiments. This excessive propagation could lead to more pessimistic assessments of how much energy can be coupled into the target volume. In this study, the self-focusing is found to be most sensitive to the thermal conductivity model for the LEH foil material and the dimensionality of the simulations. For the $2 \mu\text{m}$ thick LEH foil case, good agreement between experiments and 2D simulations was found when a tabulated thermal conductivity model was used for the LEH foil material, while 3D simulations were required to better match the $3 \mu\text{m}$ thick foil experiments. This work

gives confidence that MHD simulations are able to effectively design future MagLIF preheat configurations provided thin LEH foils and modest laser intensities are used.

ACKNOWLEDGMENTS

The authors gratefully acknowledge the outstanding support of J. Emig, D. Canning, C. Sorce, and the entire OMEGA-EP crew at the Laboratory for Laser Energetics and General Atomics for target fabrication. One of the authors (DER) was supported in part by an appointment to the Sandia National Laboratories Truman Fellowship in National Security Science and Engineering, which is part of the Laboratory Directed Research and Development (LDRD) Program, Project 209289. Sandia National Laboratories is a Multimission Laboratory managed and operated by National Technology & Engineering Solutions of Sandia, LLC, a wholly owned subsidiary of Honeywell International Inc., for the U.S. Department of Energy’s National Nuclear Security Administration under Contract No. DE-NA0003525. This paper describes objective technical results and analysis. Any subjective views or opinions that might be expressed in the paper do not necessarily represent the views of the U.S. Department of Energy or the United States Government.

APPENDIX: LASER ENERGY ABSORPTION IN PLASMAS THROUGH INVERSE BREMSSTRAHLUNG ABSORPTION

In the section, the equations describing a laser penetrating into a plasma and being absorbed through inverse bremsstrahlung are derived. We adopt the model developed in reference⁴ and further commented in Refs. 28–30. The units expressed are in mks. Light at intensity $I_0(t)$ is incident from $z = 0$, propagates toward $z > 0$ and is absorbed by inverse bremsstrahlung. The energy density $\mathcal{E}(t, z)$ of the fuel and the beam intensity I are governed by the following equations:

$$\frac{\partial}{\partial t} \mathcal{E} = -\frac{\partial}{\partial z} I = \kappa I, \tag{A1}$$

where $\kappa(t, z)$ is the absorption coefficient given by

$$\kappa(t, z) \doteq \frac{\nu_{ei} \omega_p^2}{c \omega^2} \left(1 - \frac{\omega_p^2}{\omega^2} \right)^{-\frac{1}{2}}. \tag{A2}$$

Here, c is the speed of light and ω_p is the plasma frequency and ν_{ei} is the electron–ion collision frequency given by

$$\nu_{ei} \doteq \frac{4\sqrt{2}\pi n_i Z^2 e^4 \ln\Lambda}{(4\pi\epsilon_0)^2 3\sqrt{m_e} (k_B T)^{3/2}}, \tag{A3}$$

where T is the temperature of the plasma and $\ln\Lambda$ is the Coulomb logarithm.

The absorption coefficient depends on time and space due to the changing fuel temperature. Equation (A1) can be simplified by redefining the absorption coefficient in the following manner. The fuel energy density and the fuel temperature are related by

$$\mathcal{E} = \frac{3}{2} (n_e + n_i) k_B T = \frac{3}{2} n_i (1 + Z) k_B T. \tag{A4}$$

Substituting this relation into Eq. (A2) leads to

$$\kappa(t, z) = \frac{\tilde{\kappa}}{\mathcal{E}^{\frac{3}{2}}(t, z)}, \tag{A5}$$

where $\tilde{\kappa}$ is a modified absorption coefficient

$$\tilde{\kappa} \doteq \frac{4\sqrt{2}\pi n_i Z^2 e^4 \ln\Lambda}{(4\pi\epsilon_0)^2 3\sqrt{m_e} c} \left[\frac{3}{2} n_i (1 + Z) \right]^{\frac{3}{2}} \frac{\omega_p^2}{\omega^2} \left(1 - \frac{\omega_p^2}{\omega^2} \right)^{-\frac{1}{2}}. \tag{A6}$$

Using the redefined absorption coefficient, Eq. (A1) can be rewritten as

$$\frac{\partial}{\partial t} \mathcal{E} = -\frac{\partial}{\partial z} I = \frac{\tilde{\kappa}}{\mathcal{E}^{\frac{3}{2}}(t, z)} I. \tag{A7}$$

Integrating Eq. (A7) with respect to time and assuming the internal energy of the fuel is negligible at $t = 0$, we find

$$\mathcal{E}^{\frac{5}{2}}(t, z) = \frac{5}{2} \tilde{\kappa} \Phi(t, z), \tag{A8}$$

where

$$\Phi(t, z) = \int_0^t I(z, t') dt', \tag{A9}$$

is the light fluence past a given position z . Integrating Eq. (A7) with respect to time, we also find

$$\mathcal{E} = -\partial_z \Phi. \tag{A10}$$

Substituting Eq. (A8) then gives the following:

$$\partial_z \mathcal{E}^{\frac{5}{2}} = -\frac{5}{2} \tilde{\kappa} \mathcal{E}. \tag{A11}$$

Integrating Eq. (A11) in space yields

$$\mathcal{E}^{\frac{3}{2}}(t, z) - \mathcal{E}_0^{\frac{3}{2}}(t) = -\frac{3}{2} \tilde{\kappa} z. \tag{A12}$$

In the above, we have introduced $\mathcal{E}_0(t) \doteq \mathcal{E}(t, z = 0)$ which is the energy density at $z = 0$. Note that $\mathcal{E}_0(t)$ can be directly obtained by using the result in Eq. (A8)

$$\mathcal{E}_0(t) = \left[\frac{5}{2} \tilde{\kappa} \Phi_0(t) \right]^{\frac{2}{5}}, \tag{A13}$$

where $\Phi_0(t) \doteq \Phi_0(t, z = 0)$ is the total laser fluence at $z = 0$. From these results, the energy-density profile for the fuel is

$$\mathcal{E}(t, z) = \left[\mathcal{E}_0^{\frac{3}{2}}(t) - \frac{3}{2} \tilde{\kappa} z \right]^{\frac{2}{3}}. \tag{A14}$$

To calculate the location at which a minimum temperature threshold, T_{min} , is exceeded we first define the minimum energy, \mathcal{E}_{min} , needed in a plasma required to observe such emission

$$\mathcal{E}_{min} \doteq \frac{3}{2} n_i (1 + Z) k_B T_{min}. \tag{A15}$$

To find the observed propagation length, z_* , we must solve the following equation:

$$\mathcal{E}_{min} = \left[\mathcal{E}_0^3(t) - \frac{3}{2} \tilde{\kappa} z_*(t) \right]^{\frac{2}{3}}. \quad (\text{A16})$$

Substituting the expression for \mathcal{E}_0 from Eq. (A13) leads to

$$z_*(t) = \frac{2}{3\tilde{\kappa}} \left\{ \left[\frac{5}{2} \tilde{\kappa} \Phi_0(t) \right]^{\frac{3}{5}} - \mathcal{E}_{min}^{\frac{3}{5}} \right\}. \quad (\text{A17})$$

As mentioned before, Φ_0 is the laser energy E_{laser} delivered into the gas divided by the cross sectional area σ of the laser beam. Hence, we recover the expression for the laser propagation length as follows:

$$z_*(E_{laser}) = \frac{2}{3\tilde{\kappa}} \left[\left(\frac{5\tilde{\kappa}}{2\sigma} E_{laser} \right)^{\frac{3}{5}} - \mathcal{E}_{min}^{\frac{3}{5}} \right]. \quad (\text{A18})$$

DATA AVAILABILITY

The data that support the findings of this study are available from the corresponding author upon reasonable request.

REFERENCES

- ¹S. A. Slutz, M. C. Herrmann, R. A. Vesey, A. B. Sefkow, D. B. Sinars, D. C. Rovang, K. J. Peterson, and M. E. Cuneo, *Phys. Plasmas* **17**, 056303 (2010).
- ²M. R. Gomez, S. A. Slutz, A. B. Sefkow, D. B. Sinars, K. D. Hahn, S. B. Hansen, E. C. Harding, P. F. Knapp, P. F. Schmit, C. A. Jennings, T. J. Awe, M. Geissel, D. C. Rovang, G. A. Chandler, G. W. Cooper, M. E. Cuneo, A. J. Harvey-Thompson, M. C. Herrmann, M. H. Hess, O. Johns, D. C. Lamppa, M. R. Martin, R. D. McBride, K. J. Peterson, J. L. Porter, G. K. Robertson, G. A. Rochau, C. L. Ruiz, M. E. Savage, I. C. Smith, W. A. Stygar, and R. A. Vesey, *Phys. Rev. Lett.* **113**, 155003 (2014).
- ³S. A. Slutz, M. R. Gomez, S. B. Hansen, E. C. Harding, B. T. Hutsel, P. F. Knapp, D. C. Lamppa, T. J. Awe, D. J. Ampleford, D. E. Bliss, G. A. Chandler, M. E. Cuneo, M. Geissel, M. E. Glinesky, A. J. Harvey-Thompson, M. H. Hess, C. A. Jennings, B. Jones, G. R. Laity, M. R. Martin, K. J. Peterson, J. L. Porter, P. K. Rambo, G. A. Rochau, C. L. Ruiz, M. E. Savage, J. Schwarz, P. F. Schmit, G. Shipley, D. B. Sinars, I. C. Smith, R. A. Vesey, and M. R. Weis, *Phys. Plasmas* **25**, 112706 (2018).
- ⁴J. Denavit and D. W. Phillion, *Phys. Plasmas* **1**, 1971 (1994).
- ⁵M. R. Gomez, S. A. Slutz, P. F. Knapp, K. D. Hahn, M. R. Weis, E. C. Harding, M. Geissel, J. R. Fein, M. E. Glinesky, S. B. Hansen, A. J. Harvey-Thompson, C. A. Jennings, I. C. Smith, D. Woodbury, D. J. Ampleford, T. J. Awe, G. A. Chandler, M. H. Hess, D. C. Lamppa, C. E. Myers, C. L. Ruiz, A. B. Sefkow, J. Schwarz, D. A. Yager-Elorriaga, B. Jones, J. L. Porter, K. J. Peterson, R. D. McBride, G. A. Rochau, and D. B. Sinars, *IEEE Trans. Plasma Sci.* **47**, 2081 (2019).
- ⁶A. J. Harvey-Thompson, M. R. Weis, E. C. Harding, M. Geissel, D. J. Ampleford, G. A. Chandler, J. R. Fein, M. E. Glinesky, M. R. Gomez, K. D. Hahn, S. B. Hansen, C. A. Jennings, P. F. Knapp, R. R. Pagnuio, L. Perea, K. J. Peterson, J. L. Porter, P. K. Rambo, G. K. Robertson, G. A. Rochau, D. E. Ruiz, J. Schwarz, J. E. Shores, D. B. Sinars, S. A. Slutz, G. E. Smith, I. C. Smith, C. S. Speas, and K. Whittemore, *Phys. Plasmas* **25**, 112705 (2018).
- ⁷J. D. Lindl, P. Amendt, R. L. Berger, S. G. Glendinning, S. H. Glenzer, S. W. Haan, R. L. Kauffman, O. L. Landen, and L. J. Suter, *Phys. Plasmas* **11**, 339 (2004).
- ⁸S. W. Haan, J. D. Lindl, D. A. Callahan, D. S. Clark, J. D. Salmonson, B. A. Hammel, L. J. Atherton, R. C. Cook, M. J. Edwards, S. Glenzer, A. V. Hamza, S. P. Hatchett, M. C. Herrmann, D. E. Hinkel, D. D. Ho, H. Huang, O. S. Jones, J. Kline, G. Kyrala, O. L. Landen, B. J. MacGowan, M. M. Marinak, D. D. Meyerhofer, J. L. Milovich, K. A. Moreno, E. I. Moses, D. H. Munro, A. Nikroo, R. E. Olson, K. Peterson, S. M. Pollaine, J. E. Ralph, H. F. Robey, B. K. Spears, P. T. Springer, L. J. Suter, C. A. Thomas, R. P. Town, R. Vesey, S. V. Weber, H. L. Wilkens, and D. C. Wilson, *Phys. Plasmas* **18**, 051001 (2011).
- ⁹S. H. Glenzer, D. H. Froula, L. Divol, M. Dorr, R. L. Berger, S. Dixit, B. A. Hammel, C. Haynam, J. A. Hittinger, J. P. Holder, O. S. Jones, D. H. Kalantar, O. L. Landen, A. B. Langdon, S. Langer, B. J. MacGowan, A. J. MacKinnon, N. Meezan, E. I. Moses, C. Niemann, C. H. Still, L. J. Suter, R. J. Wallace, E. A. Williams, and B. K. F. Young, *Nat. Phys.* **3**, 716 (2007).
- ¹⁰M. R. Gomez, S. A. Slutz, A. B. Sefkow, K. D. Hahn, S. B. Hansen, P. F. Knapp, P. F. Schmit, C. L. Ruiz, D. B. Sinars, E. C. Harding, C. A. Jennings, T. J. Awe, M. Geissel, D. C. Rovang, I. C. Smith, G. A. Chandler, G. W. Cooper, M. E. Cuneo, A. J. Harvey-Thompson, M. C. Herrmann, M. H. Hess, D. C. Lamppa, M. R. Martin, R. D. McBride, K. J. Peterson, J. L. Porter, G. A. Rochau, M. E. Savage, D. G. Schroen, W. A. Stygar, and R. A. Vesey, *Phys. Plasmas* **22**, 056306 (2015).
- ¹¹A. J. Harvey-Thompson, M. Geissel, C. A. Jennings, M. R. Weis, M. R. Gomez, J. R. Fein, D. J. Ampleford, G. A. Chandler, M. E. Glinesky, K. D. Hahn, S. B. Hansen, E. C. Harding, P. F. Knapp, R. R. Pagnuio, L. Perea, K. J. Peterson, J. L. Porter, P. K. Rambo, G. K. Robertson, G. A. Rochau, C. L. Ruiz, J. Schwarz, J. E. Shores, D. B. Sinars, S. A. Slutz, G. E. Smith, I. C. Smith, C. S. Speas, K. Whittemore, and D. Woodbury, *Phys. Plasmas* **26**, 032707 (2019).
- ¹²A. J. Harvey-Thompson, A. B. Sefkow, M. S. Wei, T. Nagayama, E. M. Campbell, B. E. Blue, R. F. Heeter, J. M. Koning, K. J. Peterson, and A. Schmitt, *Phys. Rev. E* **94**, 051201 (2016).
- ¹³M. M. Marinak, G. D. Kerbel, N. A. Gentile, O. Jones, D. Munro, S. Pollaine, T. R. Dittrich, and S. W. Haan, *Phys. Plasmas* **8**, 2275 (2001).
- ¹⁴M. Desjarlais, J. Kress, and L. Collins, *Phys. Rev. E* **66**, 025401 (2002).
- ¹⁵M. P. Desjarlais, *Contrib. Plasma Phys.* **41**, 267 (2001).
- ¹⁶E. M. Epperlein and M. G. Haines, *Phys. Fluids* **29**, 1029 (1986).
- ¹⁷Y. T. Lee and R. M. More, *Phys. Fluids* **27**, 1273 (1984).
- ¹⁸A. B. Sefkow, S. A. Slutz, J. M. Koning, M. M. Marinak, K. J. Peterson, D. B. Sinars, and R. A. Vesey, *Phys. Plasmas* **21**, 072711 (2014).
- ¹⁹A. J. Harvey-Thompson, A. B. Sefkow, T. N. Nagayama, M. S. Wei, E. M. Campbell, G. Fiksel, P.-Y. Chang, J. R. Davies, D. H. Barnak, V. Y. Glebov, P. Fitzsimmons, J. Fooks, and B. E. Blue, *Phys. Plasmas* **22**, 122708 (2015).
- ²⁰A. B. Langdon, *Phys. Rev. Lett.* **44**, 575 (1980).
- ²¹A simulation of the 3- μm window including the Langdon effect produced only small alterations to the laser propagation and reduced the energy coupled to the window by 30 J increasing laser penetration by $\sim 6\%$.
- ²²M. Patel, H. Scott, and M. Marinak, "The HYDRA DCA atomic kinetics package," in 52nd Annual Meeting of the APS Division of Plasma Physics (2010).
- ²³J. J. MacFarlane, I. E. Golovkin, P. Wang, P. R. Woodruff, and N. A. Pereyra, *High Energy Density Phys.* **3**, 181 (2007).
- ²⁴A. E. Mattsson and M. P. Desjarlais, *Bulletin of the American Physical Society* (American Physical Society, 2005).
- ²⁵P. F. Knapp, M. R. Gomez, S. B. Hansen, M. E. Glinesky, C. A. Jennings, S. A. Slutz, E. C. Harding, K. D. Hahn, M. R. Weis, M. Evans, M. R. Martin, A. J. Harvey-Thompson, M. Geissel, I. C. Smith, D. E. Ruiz, K. J. Peterson, B. M. Jones, J. Schwarz, G. A. Rochau, D. B. Sinars, R. D. McBride, and P.-A. Gourdain, *Phys. Plasmas* **26**, 012704 (2019).
- ²⁶J. J. MacFarlane, I. E. Golovkin, P. R. Woodruff, D. R. Welch, B. V. Oliver, T. A. Mehlhorn, and R. B. Campbell, in Proceedings of the Inertial Fusion Science Applications (2003).
- ²⁷M. Geissel, A. J. Harvey-Thompson, T. J. Awe, D. E. Bliss, M. E. Glinesky, M. R. Gomez, E. Harding, S. B. Hansen, C. Jennings, M. W. Kimmel, P. Knapp, S. M. Lewis, K. Peterson, M. Schollmeier, J. Schwarz, J. E. Shores, S. A. Slutz, D. B. Sinars, I. C. Smith, C. S. Speas, R. A. Vesey, M. R. Weis, and J. L. Porter, *Phys. Plasmas* **25**, 022706 (2018).
- ²⁸C. Constantin, C. A. Back, K. B. Fournier, G. Gregori, O. L. Landen, S. H. Glenzer, E. L. Dewald, and M. C. Miller, *Phys. Plasmas* **12**, 063104 (2005).
- ²⁹S. Y. Gus'kov, J. Limpouch, P. Nicolai, and V. T. Tikhonchuk, *Phys. Plasmas* **18**, 103114 (2011).
- ³⁰R. D. McBride and S. A. Slutz, *Phys. Plasmas* **22**, 052708 (2015).